Anti-coincidence Shielding γ-ray Detector based on $LaBr_3$(Ce)/CsI(Tl) Phoswich Scintillator*

JiFei Lu,[1] Yun Zheng,[2,†] LiHua Zhu,[1,‡] HaoTian Qi,[1] Xuan Pang,[1] Lin Song,[1] DeXing Kong,[1] BaoHua Sun,[1] TianXiao Li,[2] CongBo Li,[2] XiaoGuang Wu,[2] and JingBin Lu[3]

[1]*School of Physics, Beihang University, Beijing 100191, China*
[2]*China Institute of Atomic Energy, Beijing 102413, China*
[3]*College of Physics, Jilin University, Jilin 130012, China*

An anti-coincidence shielding γ-ray detector has been designed to study Compton suppression and cosmic rays anti-coincidence based on a $LaBr_3$(Ce)/CsI(Tl) phoswich scintillator, where the $LaBr_3$(Ce) scintillator is chosen as the main crystal completely surrounded by the CsI(Tl) scintillator. Since the differences in their pulse shapes, a series of studies have been conducted using pulse shape analysis (PSA) methods. By using digital charge integration (QDC), the energy resolutions of the detector are obtained, being 3.7% for 662 keV of ^{137}Cs , 3.1% for 1173 keV and 2.8% for 1332 keV of ^{60}Co after excluding the influence of cascade γ rays. This detector can suppress the Compton continuum by 2$\sim$5 times for ^{137}Cs/^{60}Co based on Fast and Slow Component Ratios (FCR-SCR). Furthermore, almost all cosmic rays can be rejected by filtering events above 10 MeV in an in-beam spectrum analysis. It clearly shows that this anti-coincidence shielding γ-ray detector can be used for low level radioactivity measurements as well as high energy γ rays measurements.

Keywords: phoswich detector, Compton suppression, anti-coincidence shielding, PSA, FCR-SCR

I. INTRODUCTION

In nuclear physics experiments, anti-coincidence shielding usually has two important functions: on one hand, it refers to Compton suppression, and on the other hand, it serves as shielding against cosmic rays in high-energy γ rays measurements. The Compton continuums are the main source of noise in the energy spectra which can reduce the peak-to-total (P/T) ratio of observed low-energy photopeaks and even swamp the smaller ones. Especially in the study of nuclear spectroscopy, this will reduce the sensitivity of the detection of low-energy regions and affect the accuracy of energy spectrum analysis [1]. Therefore, the suppression of the Compton continuum becomes an important factor in improving the sensitivity of low-energy regions. For example, the Compton-suppressed spectrometers made up of a high energy resolution Ge detector assisted by scintillation detectors can be used to measure γ spectra with energies lower than 2 MeV [2–5]. These scintillation detectors are arranged around the Ge detector to capture scattering events, and then veto such events during data processing, thereby achieving a cleaner energy spectrum to facilitate the analysis and research.

Moreover, effective suppression of cosmic ray backgrounds constitutes an essential requirement in a specific high-energy γ-ray detection system. γ rays with energy higher than 10 MeV are significantly influenced by cosmic rays, as the measurement efficiency for these events is very low. For example, the study of the Giant Dipole Resonance (GDR) using fusion evaporation reactions is of great significance for understanding the ground state deformation of atomic nuclei [6–10]. However, in the measurement of GDR γ spectra, the corresponding high-energy γ yield is very low, approximately $10^{-3}\sim10^{-4}$ of the neutron yield. As a result, experimental observations are severely affected by cosmic rays, making it difficult to measure accurately and even completely swamped by the cosmic ray components. In the conventional experimental setup, organic scintillator detectors are usually arranged around the main detector(such as NaI(Tl), BGO, BaF_2 and so on) to veto the cosmic ray events, thereby achieving optimal energy spectra. However, both of these traditional measurement systems have complex equipment conditions and the placement of the shielding detectors is also constrained by spatial limitations. This undoubtedly has a certain degree of inconvenience for the experiment. Today, the hardware requirements of data acquisition have been simplified greatly due to the rapid development of digital acquisition systems [11, 12]. Some inorganic scintillators with even better resolution also emerged during the same period [13]. These conditions have facilitated the development of detectors toward greater functionality and portability.

To simplify complex equipment conditions while still achieving the anti-coincidence effect, some researchers have developed novel phoswich detectors by combining all kinds of inorganic scintillators and analyzing experimental data using the pulse shape analysis (PSA) method [14], such as $LaBr_3$(Ce) + NaI [15], GAGG + CsI(Tl)[16], CsI(Tl) + BGO [17]. These types of detectors, which are aimed at Compton suppression, usually use two inorganic scintillators for the scintillation material. This is mainly because inorganic scintillators can be manufactured in various shapes and have a higher density, making them more effective at capturing Compton scattering events. Among them, the one with better resolution and relatively fast decay time is selected as the main crystal embedded in the well-typed shielding crystal and shares a PMT with performance matching the main crystal [18]. Therefore, the analysis is primarily based on events from the main crystal. In addition, an entrance window can also be implemented for improving the efficiency of capturing large-angle Compton suppression [16].

This paper presents research work related to the phoswich

* Supported by the National Natural Science Foundation of China (Nos. U1867210, U2167201 and U2167292)

† Corresponding author, zhengyun@ciae.ac.cn
‡ Corresponding author, zhulh@buaa.edu.cn

detector to realize both Compton suppression and cosmic rays anti-coincidence, which utilizes the $LaBr_3$(Ce)/CsI(Tl) scintillator combinations. The $LaBr_3$(Ce) scintillator is chosen as the main crystal because of its excellent energy resolution ($\sim$3% for 662 keV) and fast decay time($\sim$16 ns)[19]. The CsI(Tl) scintillator serving as the shielding crystal has a high effective Z and density, allowing it to effectively capture scattering events. Moreover, its decay time ($\sim$1000 ns) is much longer than that of $LaBr_3$(Ce), making pulse shape discrimination (PSD) easier [20]. The effect of Compton suppression in the low energy region was carefully studied by using pulse analysis methods. Furthermore, an in-beam experiment of the fusion evaporation reaction (52 MeV ^{11}B+^{142}Ce) was conducted to verify the anti-coincidence of cosmic rays in the high energy region. The content consists of the following components:

Section II presents the principle of the phoswich detector and the design of the $LaBr_3$(Ce)/CsI(Tl) phoswich scintillator. In Sect. III, we introduce the experiments and results, including ^{60}Co/^{137}Cs measurements and the in-beam measurement. In Sect. IV, we discuss the energy resolution of cascade γ rays, the ability of Compton suppression, and cosmic rays anti-coincidence. A summary is provided in Sect. IV.

II. METHOD AND SETUP

A. Principle of the phoswich detector

For an anti-coincidence shielding phoswich detector, the main crystal is usually surrounded by a shielding crystal [15]. The schematic diagram of the phoswich detector is shown in Fig. 1. The shape of the main crystal (blue) is cylindrical while the shield crystal should be well-typed (yellow). In order to capture scattering events in a 4π space, there is also an entrance window (dark yellow). Both of these two scintillators share only one PMT that is suitable for the main crystal. Therefore, the results of the analysis tend to the characteristics of the main crystal.

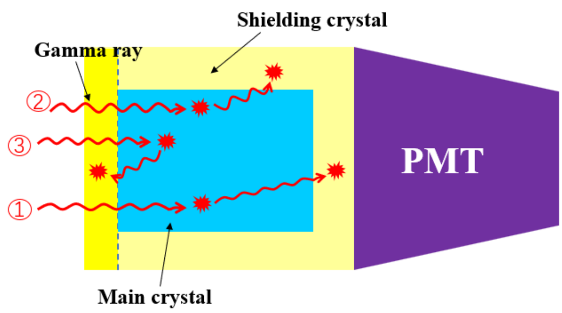

Fig. 1. Schematic diagram of the phoswich detector.

The shielding crystal has two important characteristics: 1)The part of it located between the main crystal and the PMT window can be used to capture small-angle scattering events. 2) The entrance window of it helps to capture back-scattering events. However, the entrance window will have a certain absorption effect on γ rays, reducing the peak-to-total ratio of the main crystal and affecting the measurement efficiency [21].

Unlike traditional analog circuitry for acquiring data, this phoswich detector requires a digital acquisition system to collect pulses and use PSA methods to distinguish events between three types of crystals [22]. The output pulses can be accurately described by Eq. 1 without considering the PMT time fluctuations [23].

$$V(t) = \begin{cases} -\frac{GNeR}{\tau-\tau_s}[e^{-\frac{t}{\tau_s}} - e^{-\frac{t}{\tau}}] & \text{if } \tau \neq \tau_s \\ (\frac{GNeR}{\tau_s^2}) \cdot t \cdot e^{-\frac{t}{\tau_s}} & \text{if } \tau = \tau_s \end{cases} \quad (1)$$

Where G, e, R represent the gain of the PMT, charge of the electron and the resistance in the circuit, respectively; N represents the number of photoelectrons emitted by the cathode, proportional to the product of energy and light yield; τ_s and τ represent the decay time of the scintillator and the output circuit time constant, respectively. Table 1 provides a comparison of various typical inorganic scintillators, including density, maximum emission wavelength and fluorescence decay time [19, 24]. By analyzing the pulses of these common scintillators through calculations, suitable selections can be determined.

Table 1. Properties of commonly used typical inorganic scintillation crystals.

Material	Density (g/cm^3)	λ_{max} (nm)	Decay time (ns)	Light yield (Ph/MeV)
NaI(Tl)	3.67	415	230	38000
CsI(Tl)	4.51	550	1000	54000
BGO	7.13	480	300	9000
GAGG	6.63	520	100	56000
LSO	7.4	420	40	27000
$LaBr_3$(Ce)	5.29	358	16	61000
GSO	6.7	440	60	12500

By setting the τ constant to 20 ns and the same energy condition in the calculation, the pulses for different crystals were formulated using Eq. 1 shown in Fig. 2. The τ is set so short to ensure that the pulse reflects its decay time characteristics in the falling edge, which is beneficial for shape discrimination.

From Fig. 2, it is evident that crystals with short decay times and high light yields generate tall and narrow pulses, whereas those with long decay times and low light yields produce short and wide pulses. The differences in pulse characteristics among various crystals are crucial for realizing PSD.

B. Pulse Analysis Method

Since the phoswich detector has two scintillators, it outputs pulses of different shapes that need to be discriminated. One method called Fast and Slow Component Ratios (FCR-SCR) can be used to separate pulses with different falling edges,

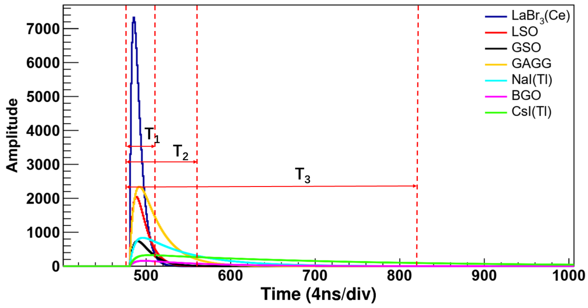

Fig. 2. The pulses for different scintillators formulated by Eq. 1. Different intervals marked as T_1, T_2, and T_3 are also shown for integration.

which is based on the Charge Comparison Method (CCM). Taking Fig. 2 as an example, the pulses are divided into different integration segments by setting different time nodes within the time window. To calculate values of the fast component ratio (FCR) and slow component ratio (SCR) of each pulse, first determine the starting point, which is before the pulse trigger point. Then, integrate over intervals T_1, T_2, and T_3 to obtain the integral values S_1, S_2, and S_3 for each interval, respectively. The intervals are set according to the pulse width of the main crystal. Finally, the FCR and SCR can be obtained by the following equation.

$$FCR = \frac{S_1}{S_2} \tag{2}$$

$$SCR = \frac{S_2}{S_3} \tag{3}$$

It is worth noting that Eq. 3 is a modified version of the formula from [14]. The appropriate choice of the integration range can reduce the effect of baseline fluctuations on the integration results in practice. Since there is an inclusion relationship among S_1, S_2, and S_3, the range of both FCR and SCR is 0 $\sim$ 1.

Fig. 3 shows the distribution of different scintillators in the FCR-SCR two-dimension plot. The integral values of T_1, T_2, and T_3 are 120 ns, 240 ns, and 1200 ns, respectively. In this condition, integral segment T_1 can almost fully integrate the $LaBr_3$(Ce) pulse, so its values of the FCR or the SCR are near 1. From Fig. 3, the $LaBr_3$(Ce) scintillator and CsI(Tl) scintillator can be selected as an excellent combination for the phoswich scintillator because of the excellent discrimination between them.

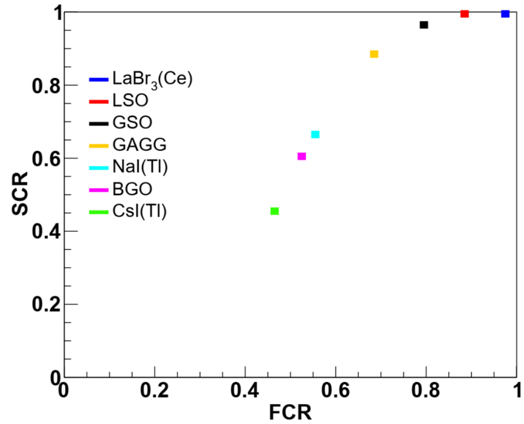

Fig. 3. Distribution of different scintillators in the FCR-SCR two-dimension plot.

C. The $LaBr_3$(Ce)/CsI(Tl) phoswich Scintillator

The schematic diagram of the $LaBr_3$(Ce)/CsI(Tl) phoswich scintillator is shown in Fig. 4a based on the design concept in Fig. 1. The inner $LaBr_3$(Ce) cylindrical crystal has a height of 5.0 cm and a radius of 1.9 cm. It is embedded in the well-typed CsI(Tl) crystal, which has a height of 7.0 cm (including a 1.0 cm thick top layer) and a radius of 3.8 cm. The optical silicon grease coupling of the EJ550 model is used between crystals to ensure optical transmission between them.

The image of the phoswich detector is shown in Fig. 4b after encapsulation. The selected photomultiplier tube (PMT) model is Hamamatsu's R6233, with a matching voltage divider model E1198-27. The detector is enclosed in a magnetic shielding case of model E989-15 and provides some shade. τ ($\sim$23 ns) of this PMT base is fast, making it suitable for the $LaBr_3$(Ce) scintillator. The outer silver-white aluminum casing also provides some electron absorption.

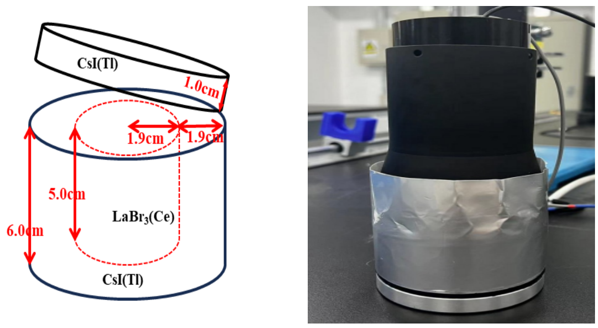

Fig. 4. (a) Schematic diagram of the $LaBr_3$(Ce)/CsI(Tl) phoswich scintillator; (b) Image of the phoswich detector.

The prediction of the phoswich detector pulses is shown in Fig. 5a. Among them, the $LaBr_3$(Ce) pulse is represented in black, the CsI(Tl) pulse in blue, and the $LaBr_3$(Ce)+CsI(Tl) pulse in red. The latter is also referred to as the "coincidence pulse". The τ set during the calculation process is 20 ns to match $LaBr_3$(Ce) decay time. Therefore, the CsI(Tl) pulse will be significantly less than the $LaBr_3$(Ce) pulse in terms of amplitude. It is also seen that the tail of the coincidence pulse is from the contribution of CsI(Tl) and the front part mainly from $LaBr_3$(Ce). In the calculation, the energy of $LaBr_3$(Ce) deposition is set to 1.173 MeV and the energy of CsI(Tl) de-

position to 1.332 MeV, and the coincidence pulse is the sum of the two. The pulses from the experiment correspond to the same energy shown in Fig. 5b. The calculation results agree well with the experimental results except a certain amount of jitter in the experimental pulses.

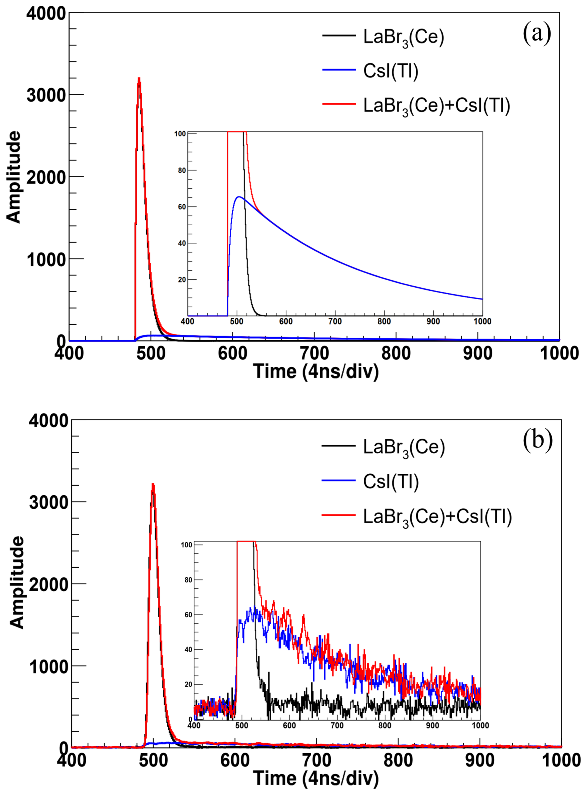

Fig. 5. (a) Three types of pulses of the phoswich detector predicted from Eq. 1. (b) Three types of pulses of the phoswich detector from the experiment. Black: $LaBr_3$(Ce) pulse; Blue: CsI(Tl) pulse; Red: $LaBr_3$(Ce)+CsI(Tl) pulse. Inserted figure: expansion plot showing the pulse tail contributed from CsI(Tl).

III. EXPERIMENTS AND RESULTS

The general-purpose digital data acquisition system (GDDAQ) developed by Peking University is used for data collection in our work [25–27]. This system consists of 16 channels, each operating at a sampling rate of 2.5 million samples per second (250 MSPS), with incoming pulses digitized at 14-bit resolution. The properties of GDDAQ make it suitable for collecting $LaBr_3$(Ce) pulses. Using FPGA for pulse processing greatly simplifies equipment requirements and improves data acquisition efficiency [28].

The experimental diagram shown in Fig. 6 depicts the setup where the two ends of the detector are connected. One end is attached to a positive high voltage, while the other end is connected to a GDDAQ. Under the logic control of the FPGA (trigger/filter), the analog pulse is converted by the ADC into a digital pulse that is convenient for storage and analysis. The total time window for each pulse collection is set to 10 μs, with a pulse trigger delay of 2 μs. This set ensures that the time window is sufficiently long to capture the pulse from the CsI(Tl) crystal (τ = 1000 ns) during each pulse acquisition. Considering the fluctuation of noise, the baseline is usually set at 10% of the maximum range, rather than at the zero position. We primarily store the acquired pulses to analyze flexibly in the later stage at each measurement.

A. ^{60}Co and ^{137}Cs Measurements

The phoswich detector was tested using radioactive sources including ^{60}Co (1.92 μCi) and ^{137}Cs (1.94 μCi) with the voltage set to +850 V. The radiation sources is positioned about 30 cm from the detector's front surface, with count rates approximately 600 counts per second (cps) for ^{60}Co and 650 cps for ^{137}Cs.

1. Pulse Shape Discrimination

A total of 170K events were accumulated from the ^{137}Cs radioactive source to analyze and discriminate three types of pulses from the phoswich detector. The source was placed in front of the detector during the measurement. These three types of pulses obtained under the voltage condition are shown in Fig. 5b.

To achieve excellent anti-coincidence effects, the integration interval widths for T_1, T_2, and T_3 are set at 120 ns, 240 ns and 1200 ns in accordance with our calculations. The scatter plot of the FCR-SCR two-dimension plot for ^{137}Cs is clearly presented in Fig. 7. Region 1, 2 represent single events in $LaBr_3$(Ce), CsI(Tl). Region 3 shows coincidence events of $LaBr_3$(Ce) and CsI(Tl). The scattered data distribution in other regions primarily consists of two or more pulses detected within the event window because of the accidental coincidence. Events in region 3 closer to region 1 have shapes more similar to those of $LaBr_3$(Ce) pulses. Conversely, events farther from region 1 are similar to the shapes of CsI(Tl) pulses. From Fig. 7, we end up realizing that anti-coincidence only requires selecting our desired $LaBr_3$(Ce)-only events from the total events.

2. Energy Spectra

Although the $LaBr_3$(Ce) crystal exhibits relatively high detection efficiency and reasonable energy resolution compared to other typical scintillation crystals, it has internal radiation due to the natural abundance of ^{138}La and ^{227}Ac decay products, which contribute to the inevitable background events [29–31]. The background count rate is about 80 cps and its characteristic peaks will appear in the energy spectra.

The energy spectra are obtained using QDC. The integration interval width is set to 120 ns, allowing for nearly full integration of the pulses captured by the $LaBr_3$(Ce) scintillator. Energy calibration is performed based on the channels of the $LaBr_3$(Ce). The results are shown in Fig. 8. Each figure

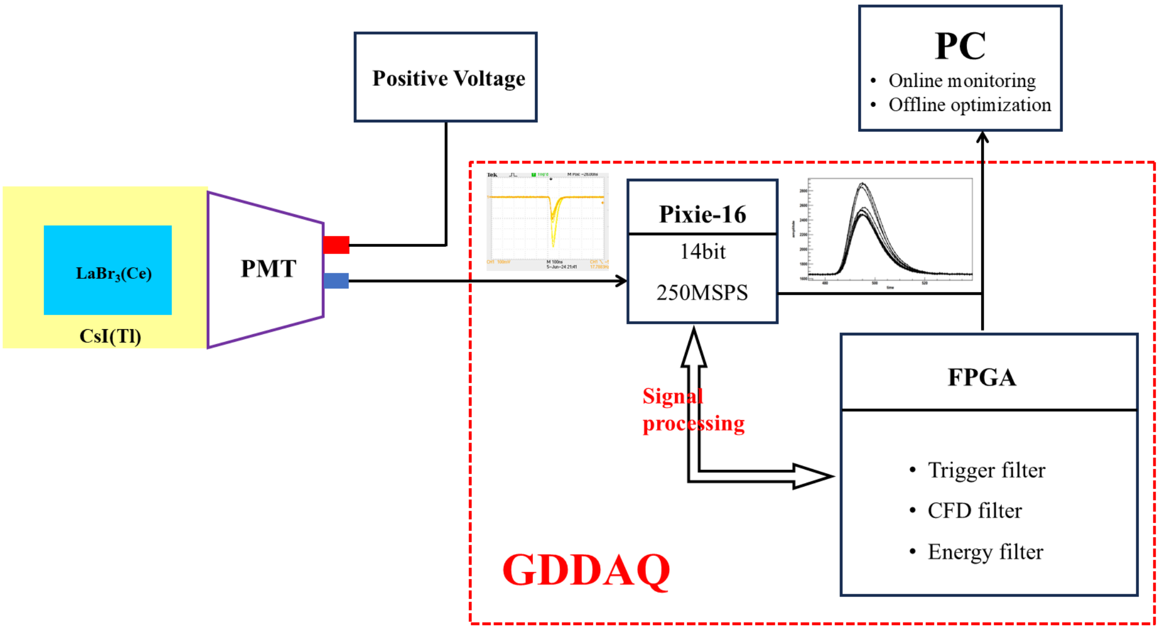

Fig. 6. Diagram of the digital data acquisition system.

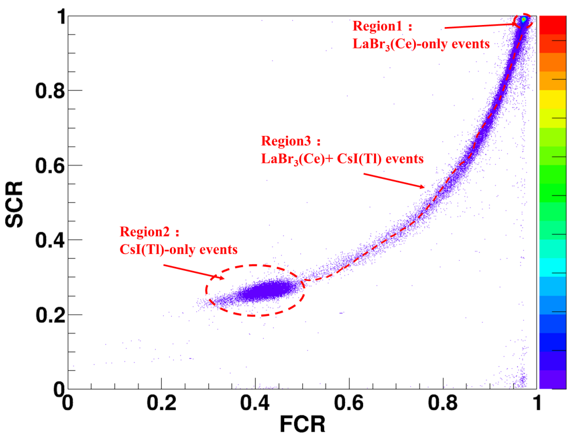

Fig. 7. Scatter plot of the FCR-SCR two-dimension plot for ^{137}Cs. Region 1 consists of $LaBr_3$(Ce)-only events, Region 2 consists of only CsI(Tl)-only events, and Region 3 consists of "$LaBr_3$(Ce)+CsI(Tl)" events (coincidence).

contains four energy spectra, including the raw spectrum, the spectrum after Compton suppression, the CsI(Tl)-only spectrum and the coincidence events spectrum. It can be seen that the CsI(Tl) events are concentrated at the low-energy end and form distinct peaks. Moreover, the characteristic peaks of 1436 keV γ and α emitter contaminants are still presented in both figures. By selecting the intervals where FCR ≥ 0.97 and SCR ≥ 0.96 from Fig. 7, the spectrum after Compton suppression is obtained. The energy resolutions of this detector are 3.7% (∼662 keV), 3.1% (∼1173 keV), 2.8% (∼1332 keV) before and after Compton suppression.

However, when the radioactive source is placed at 5 cm away from the detector, the ^{60}Co energy spectrum after Compton suppression will be narrow at the photopeaks, while ^{137}Cs does not exhibit this feature shown in Fig. 8 inserted figures. The energy resolutions are 3.8% for 662 keV, 3.7% for 1173 keV and 3.2% for 1332 keV before Compton suppression in the distance of 5 cm. After Compton suppression, the energy resolutions are 3.8% for 662 keV, 3.1% for 1173 keV and 2.8% for 1332 keV. These results indicate an energy resolution worsening between 17% and 11% at the ^{60}Co spectrum. Only by increasing the distance can the phenomenon be eliminated, which will be discussed in Sect. IV A.

B. In-beam measurement

In order to benchmark the effect of cosmic anti-coincidence in the high-energy γ rays range of the phoswich detector, we also conducted an in-beam measurement. A fusion evaporation reaction experiment was conducted at the China Institute of Atomic Energy. The experiment measured the reaction ^{11}B + ^{142}Ce at E_{beam} = 52 MeV, with our detector placed at 60 degrees parallel to the beam line and a distance of 25 cm from the target within reasonable limits of space. The core goal of the measurement spectrum is mainly focused on the γ rays above 10 MeV, which correspond to GDR γ rays. The data acquisition system still used GDDAQ for collection, with the voltage adjusted to +600 V to ensure that high-energy pulses could be captured within the dynamic range. In the beam experiment measurement, the overall count rate fluctuated within the range of 3000 $\sim$ 4500 cps. Approximately 2.45×10^{8} pulses were collected by measuring for 23 hours.

As shown in Fig. 9, the blue energy spectrum represents

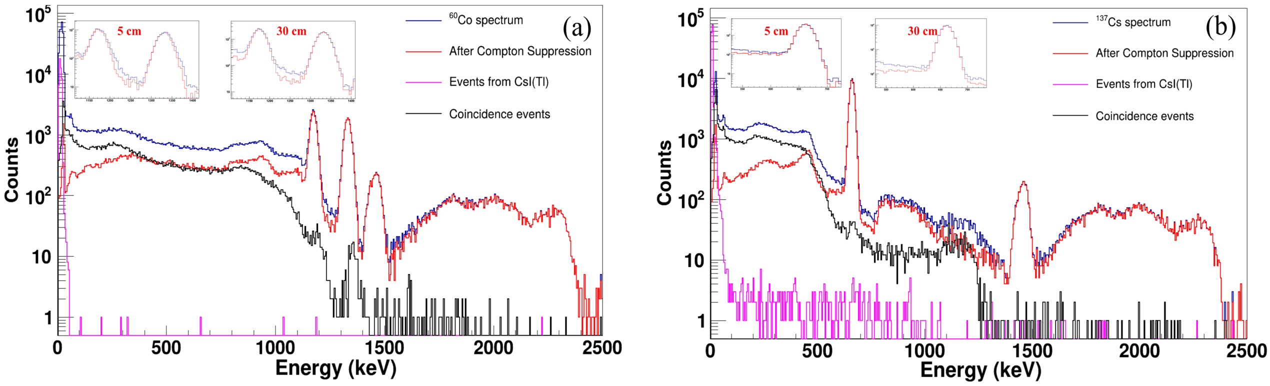

Fig. 8. The spectra from ^{60}Co and ^{137}Cs. The distance is 30 cm between the radioactive source and the surface of the detector. Inserted figure: The photopeak spectrum at different distances.

the in-beam spectrum, while the red spectrum corresponds to the blue one after anti-coincidence. Since the low collection efficiency in the high-energy region (>10 MeV), most of the pulse data is concentrated below 2 MeV, with a difference of 5 to 6 orders of magnitude. Even with a broader bin width, some characteristic peaks can still be observed below 2 MeV, and they become even more distinct after anti-coincidence. We have also measured the background spectrum in our laboratory (black one) with the same time, and the magenta one is the γ-only background spectrum after anti-coincidence. Additionally, we used Geant4 to simulate the muon energy spectrum and the decay of ^{138}La/^{227}Ac in the detector to confirm that the peak in the high-energy region originates from cosmic rays, and the results were well confirmed (green one). The simulation above 20 MeV is higher than the experimental results from the fact that we do not have an ideal setup for realistic environments.

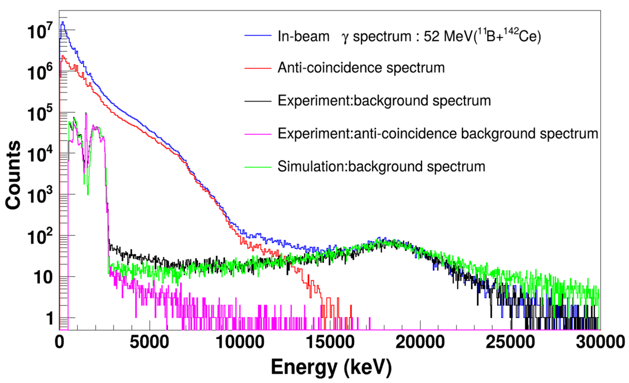

Fig. 9. Energy spectra from in-beam, background and Geant4 simulation. Blue: The raw spectrum from in-beam experimental measurements. Red: The in-beam spectrum after anti-coincidence. Black: The background spectrum from experiment. Magenta: The background spectrum after anti-coincidence. Green: The background spectrum from Geant4 simulation.

IV. DISCUSSION

A. Energy resolution of cascade γ-rays

In Fig. 8, we measured the energy spectrum with the radioactive source at different distances. We found that the energy resolution of cascade γ rays degrades when the source is close to the detector but improves after Compton suppression. The scatter plots of SCR-Energy two-dimension plot would help us analyze this phenomenon. As shown in Fig. 10a and Fig. 10b, they provide both energy information on the x-axis and the distribution of different types of events on the y-axis from the experiment. Taking Fig. 10a as an example, we think the LaBr$_3$(Ce)-only events are distributed in SCR > 0.96, the CsI(Tl)-only as SCR < 0.3, and others are coincidence events. In addition, line-1 and line-2 represent the 1173 keV and 1332 keV γ rays continuously undergoing multiple Compton scattering in the LaBr$_3$(Ce) crystal and captured by the CsI(Tl) crystal until they are all deposited in CsI(Tl). The reason why the two trends eventually merge in the CsI(Tl)-only events and cannot be distinguished is that the QDC selection range is not properly adapted for the CsI(Tl) pulses. Line-3 is from the sum peak, so it is inferred that the total energy in the phoswich detector is 2505 keV in region 1 (two dark dots). This indicates that both crystals simultaneously captured the two cascade γ rays. The pulses in the previous Fig. 5b were also picked from these regions discussed based on Fig. 10a. Fig. 10a also clearly demonstrates the energy deposition characteristics of γ rays entering the phoswich detector. Maybe they are all in LaBr$_3$(Ce), maybe they are all in CsI(Tl), or maybe they are more likely that Compton scattering occurs in one to be captured by the other completely or partly. Since the SCR interval for Compton suppression is selected to be above 0.96, it can be seen that the narrowing of the photopeak after suppression is caused by region 1 (Fig. 7). However, Fig. 10b shows a very clean distribution compared with Fig. 10a because of the single γ ray of ^{137}Cs.

In order to better understand the reasons for optimizing energy resolution after Compton suppression, the Geant4 simu-

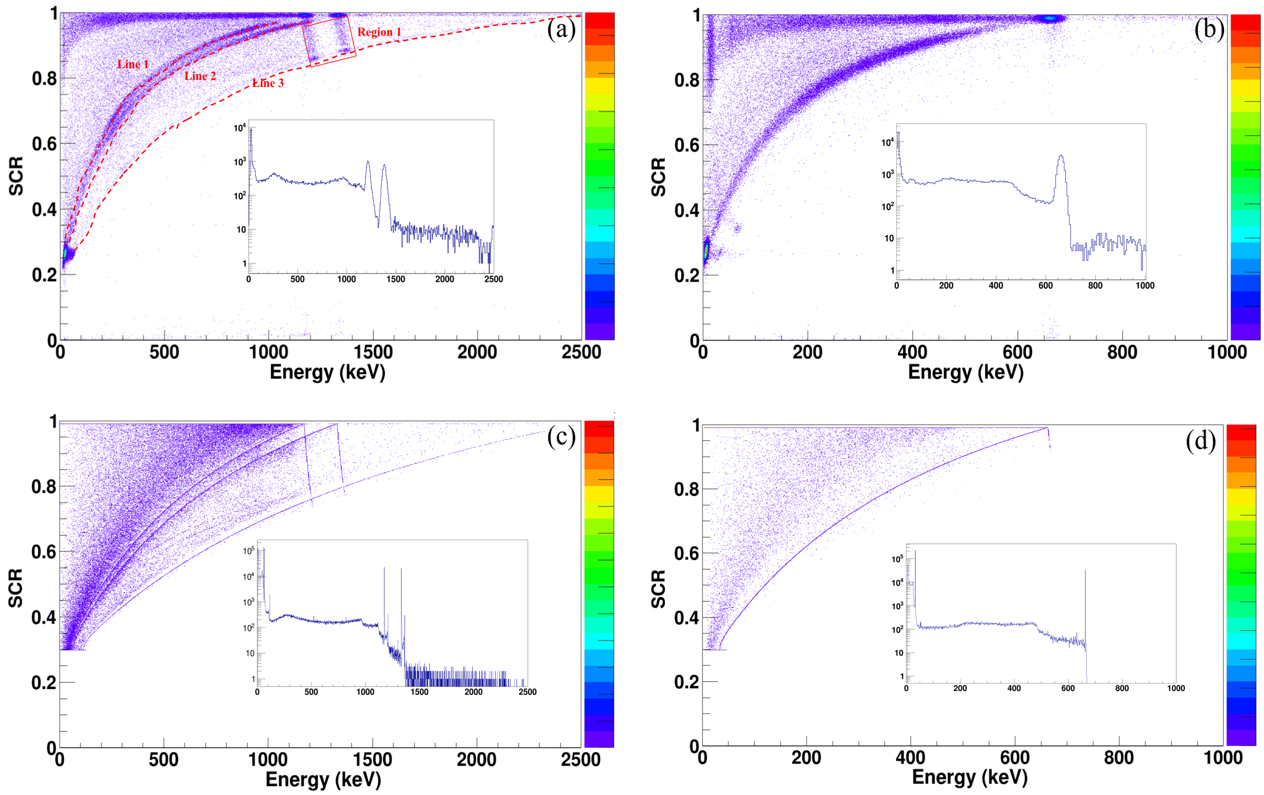

Fig. 10. Scatter plots of SCR-Energy two-dimension plot from experiments (top panel) and simulations (bottom panel) for ^{60}Co (a and c) and ^{137}Cs (b and d). The radiation source is 5 cm away from the surface of the detector. Inserted figure: energy projection spectrum.

lation is used to help analyze the experimental data because it can output physical information [32, 33]. We obtained the energy deposition results through simulation and converted them to a pulse using Eq. 1, for which the pulses are consistent with the experimental results (Fig. 5). The simulated PSA scatter plots are shown in Fig. 10c and Fig. 10d. Similar to region 1 in Fig. 10a, this phenomenon suggests that the $LaBr_3$(Ce) crystal captures one γ, while the CsI(Tl) crystal captures the other. Specifically, when this phoswich detector was exposed to the ^{60}Co radiation source with a strong cascading effect, the coincident events at 1173 keV and 1332 keV between the two scintillators were clearly observed. For example, the 1173 keV γ ray was captured by the $LaBr_3$(Ce) scintillator, while the 1332 keV cascade γ ray was captured by the CsI(Tl) scintillator. So, they will eventually converge on line-3. The energy projection spectrum for ^{60}Co simulation without energy broadening in Fig. 10c inserted figure shows one peak appear after each photopeak. After broadening, such events are swamped by the tail of the photopeak, which worsens the resolution; therefore, the energy resolution will be optimized after excluding the influence of cascade γ rays (Sec. III A 2). However, the QDC integration width is the primary cause of this phenomenon. A wider integration width can partially mitigate the effect of CsI(Tl) events on the $LaBr_3$(Ce) photopeak's energy resolution, but the ability to distinguish between the two pulses deteriorates. In conclusion, the phoswich detector's energy resolution for cascade γ rays decreases when the radiation source is close. The energy resolution will become better when the radioactive source is pulled away from the distance because the probability of capturing these two γ rays decreases.

B. Compton suppression

We present the energy spectra measured using the ^{60}Co source and the ^{137}Cs source, and extract the spectra of different events using the FCR-SCR method in Fig. 8. After Compton suppression, the events in the Compton continuum are significantly reduced. For Compton continuum, we defined the energy range as 170 $\sim$ 490 keV for 662 keV; 210 $\sim$ 963 keV for 1173 keV; and 214 $\sim$ 1118 keV for 1332 keV from the back-scattering peak to the Compton edge [34]. The Compton suppression factor can be defined as the following:

$$\zeta = \frac{I_{us}}{I_s} \times 100\% \tag{4}$$

where ζ is the suppression factor. I_{us} is the number of counts in energy E of the unsuppressed spectrum and I_s is the number of counts in energy E of the suppressed spectrum. The higher the value of ζ, the more ideal the suppression effect. As shown in Fig. 11, in order to highlight the count

variation at the photopeak position, the energy interval selection range is appropriately extended from the Compton continuum to the photopeak. In the Compton continuum, 50 bins are selected as one point, and the error bar for each point is obtained using the error propagation formula.

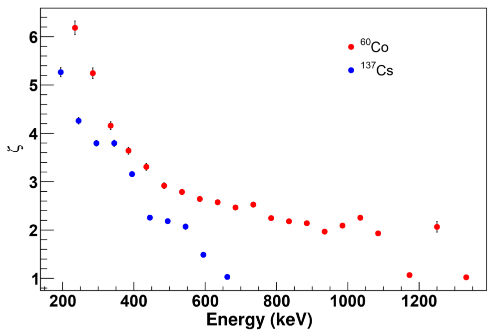

Fig. 11. The Compton suppression factor of the phoswich detector for ^{60}Co (red dots) and ^{137}Cs (blue dots).

From Fig. 11, it can be seen that the value of ζ is close to 1 at the photopeaks position, indicating that there is almost no loss at the photopeaks (the suppression factors are 1.04 for 662 keV; 1.06 for 1173 keV; 1.02 for 1332 keV). There is a certain suppression effect between the two photopeaks of ^{60}Co, likely due to scattering from the 1436 keV photopeak (Fig. 10). The suppression factor has significantly increased in the Compton continuum due to the effective suppression. For the photopeak of ^{137}Cs, the suppression in this energy region ranges from 2$\sim$5 times. For the two photopeaks of ^{60}Co, the suppression effect of the Compton continuum reaches 2$\sim$6 times. Due to the detector's structural design, a 1.0 cm thick CsI(Tl) top layer is added near the radiation source to capture back-scattering events. Therefore, as can also be seen from the Fig. 11, a certain degree of suppression effect is also achieved in the Compton edge (corresponding to back-scattering events). The suppression effect of the low-energy part in the Compton continuum is more effective than that of the high-energy part. This indicates that small-angle scattering events have a higher detection efficiency compared with back-scattering events.

C. Cosmic rays anti-coincidence

As shown in Fig. 9, the γ rays with energy more than 10 MeV are completely buried by cosmic rays and cannot be observed in the in-beam spectrum. As we all know, atmospheric cosmic ray muons constantly pass through the detector, causing energy loss within it, and the incident muons follow a zenith angle distribution from top to bottom [35, 36]. For the phoswich detector, muons entering from top to bottom will generate two types of pulses: 1) Only CsI(Tl) crystal capture; 2) Captured by both CsI(Tl) and $LaBr_3$(Ce) crystals. As shown in Fig. 12, in terms of the pulse amplitude and width, the muon pulse shows a clear distinction from the γ pulse. Therefore, by using the FCR-SCR method to select the $LaBr_3$(Ce)-only events, we can effectively filter out the components from cosmic rays in the energy spectrum.

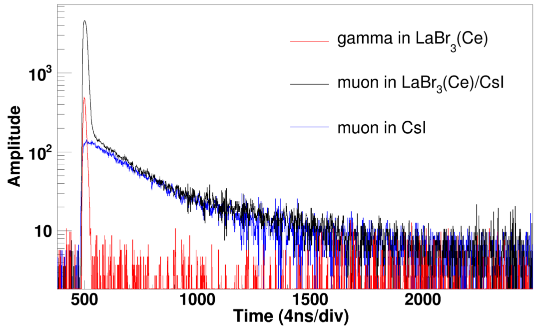

Fig. 12. Pulse comparison of muon with γ measured in the phoswich detector in the phoswich detector. Red: γ rays interacting only with the $LaBr_3$(Ce) crystal; Black: muon interacting with both crystals; Blue: muon interacting only with the CsI(Tl) crystal.

The resulting energy spectrum is shown as the red spectrum in Fig. 9 after selecting the $LaBr_3$(Ce)-only events. For energy greater than 10 MeV in the background spectrum, there are about 14, 600 events before anti-coincidence, while only 60 events remained after anti-coincidence. This means that almost all cosmic rays can be rejected. Therefore, the suppression effect will also be reflected in the in-beam spectrum because of the same measured time in the high-energy region. Due to the effective anti-coincidence effect of the background spectrum, the in-beam spectrum presents a 'bump' above 10 MeV which is characteristic of GDR γ after anti-coincidence [37]. This fully demonstrates that, under the characteristics of the structure, cosmic rays can be eliminated by means of PSA and it can be used to study high-energy γ such as GDR γ rays spectrum. In experiments, the CASCADE program, based on statistical model theory, is commonly used to fit the observed high-energy γ spectra and extract the GDR parameters (resonance energy E; shape width Γ; strength S) [37, 38]. This could be a point for future research, but it is essential to ensure a sufficient amount of measurement data.

V. SUMMARY

We introduced a novel anti-coincidence shielding phoswich detector which consists of the $LaBr_3$(Ce) and CsI(Tl) scintillator. The $LaBr_3$(Ce) scintillator is selected as the main crystal and the CsI(Tl) scintillator as the shielding crystal, so it can realize excellent discrimination of pulses to achieve the anti-coincidence. In the experiment, pulses were collected using the GDDAQ, energy spectra were obtained via the QDC, and pulse discrimination was performed using the FCR-SCR method. Since the integration width of the selected region is determined by the $LaBr_3$(Ce) pulse width in QDC calculations, CsI(Tl) events are primarily concentrated in the low energy region of the spectrum in the radioactive source measurement. The energy resolution of the detector is 3.7% for 662 keV of ^{137}Cs, while achieving 3.1% for 1173 keV and 2.8% for 1332 keV of ^{60}Co after excluding

the influence of cascade γ rays. The detector suppresses the Compton continuums of ^{60}Co/^{137}Cs by a factor of 2$\sim$5 times with almost no loss of the photopeaks. Furthermore, we conducted an experiment focusing on the high-energy γ rays (> 10 MeV) emitted in the fusion evaporation reaction ^{11}B + ^{142}Ce at E_{beam} = 52 MeV in order to study the shielding effect of cosmic rays. We successfully applied the PSD to mitigate the impact of high-energy cosmic rays and almost all cosmic rays can be rejected by filtering events above 10 MeV. After the anti-coincidence process, the energy spectrum clearly displayed the 'bump' feature of the GDR γ rays.

This phoswich detector not only can suppress the Compton continuum, which is crucial for enhancing measurement sensitivity in some low level radioactivity measurements, but also realizes anti-coincidence shielding of cosmic rays in the high-energy range, such as the measurement of high-energy γ rays such as GDR γ rays.

---

[1] S.Bender, B.Heidrich, Ünlü K., Compton suppressed $LaBr_3$ detection system for use in nondestructive spent fuel assay. Nucl. Instrum. Methods Phys. Res. A. **784**, 474-481 (2015). doi: https://doi.org/10.1016/j.nima.2014.12.025

[2] J. Parus, J. Kierzek, W. Raab, *et al.*, A dual purpose Compton suppression spectrometer. J. Radioanal. Nucl. Chem.**258**, 123-132(2003).https://doi.org/10.1023/a:1026270428392

[3] Y. Li, W.D. Huang, S.H. Shi, *et al.*, The level structure of ^{76}Se from ^{76}Br γ-decay. Nucl. Sci. Tech. **9**, 199-208(1998).

[4] De Voigt M J A, Bacelar J C, Micek S L, *et al.*, A novel compact Ge-BGO Compton-suppression spectrometer.Nucl. Instrum. Methods Phys. Res. A. **356**, 362-375(1995).https://doi.org/10.1016/0168-9002(94)01204-0

[5] Tabor S L, BGO suppressed gamma detector arrays.Nucl. Instrum. Methods Phys. Res. B.**24** 1031-1034(1987).https://doi.org/10.1016/S0168-583X(87)80305-1

[6] Zhu L, Huang Z, Hou L, *et al.*, Study of Giant Dipole Resonance in Hot Rotating Nucleus ^{132}Ce.Chin. Phys. Lett.**12**, 148-151(1995).10.1088/0256-307X/12/3/006

[7] Spicer, B.M., The Giant Dipole Resonance. Adv. Nucl. Phys.(1969).https://doi.org/10.1007/978-1-4684-8343-7_1

[8] Krasznahorkay A J, Krasznahorkay A, Csatlós M, *et al.*, An Update of the Hypothetical X17 Particle.Universe. **10**, 409-(2024).https://doi.org/10.3390/universe10110409

[9] Mason, W.M., Kernel, G., Black, J.L., *et al.*, The giant dipole resonance and isospin in$^{89}\gamma$(p, γ)^{90}Zr.Nucl. Phys.A.**135**, (1969).https://doi.org/10.1016/0375-9474(69)90158-4

[10] B. L. Berman and S. C. Fultz, Measurements of the giant dipole resonance with monoenergetic photons.Rev. Mod. Phys.**47**, 713(1975).https://doi.org/10.1103/RevModPhys.47.713

[11] Warburton W K, Grudberg P M., Current trends in developing digital pulse processing electronics for semiconductor detectors.Nucl. Instrum. Methods Phys. Res. A.**568**, 350-358(2006).https://doi.org/10.1016/j.nima.2006.07.021

[12] Koskelo M J, Koskelo I J, Sielaff B., Comparison of analog and digital pulse processing systems using pulsers.Nucl. Instrum. Methods Phys. Res. A.**422**, 373-378(1999).https://doi.org/10.1016/S0168-9002(98)00986-3

[13] J.Glodo, W.W.Moses, Effects of Ce Concentration on Scintillation Properties of $LaBr_3$:Ce.IEEE Trans. Nucl. Sci. **52**, 1805-1808(2005).10.1109/NSSMIC.2004.1462374

[14] Min, Sujung, Bumkyung Seo, Changhyun Roh, *et al.*, phoswich Detectors in Sensing Applications. Sensors. **21**, 4047(2021). https://doi.org/10.3390/s21124047

[15] H.D.Wang, Jing-Bin Lu, R.P. Li, *et al.*, A phoswich design using real-time rise time discrimination for Compton suppression of LaBr3:Ce detector.Nucl.Instrum. Methods Phys.Res.A, **1048**:167920(2023). https://doi.org/10.1016/j.nima.2022.167920

[16] H.D.Wang, Jing-Bin Lu, R.P.Li, *et al.*, An entrance window surrounded phoswich design for efficient large-angle Compton-suppressed and low-background GAGG: Ce detector.Nucl. Instrum. Methods Phys.Res.A, **1055**:168542(2023). https://doi.org/10.1016/j.nima.2023.168542

[17] Farsoni, A.T., Alemayehu, B., Alhawsawi, A. *et al.*, A compton-suppressed phoswich detector for gamma spectroscopy.J Radioanal Nucl Chem, **296**, 63–68 (2013). //doi.org/10.1007/s10967-012-2009-2

[18] Jia Xu, Jun Liu, Xiulian Chen, A well typed phoswich detector consisting of CsI and plastic scintillators for low level radioactivity measurements.Appl. Radiat. Isot.**169**, 109462(2021). https://doi.org/10.1016/j.apradiso.2020.109462

[19] Paul Lecoq, Development of new scintillators for medical applications.Nucl. Instrum. Methods Phys.Res.A.**809**, 130-139(2016). https://doi.org/10.1016/j.nima.2015.08.041

[20] LI Tianxiao, Wu Hongyi, Zheng Yun, *et al.*, Study on Compton-suppressed phoswich Gamma-ray Detector of $LaBr_3$(Ce)-CsI(Tl).Nucl. Phys. Rev.**40**, 73-77(2023). doi: 10.11804/NuclPhysRev.40.2022021

[21] Davission C M, Gamma-Ray Absorption Coefficients.Mod. Phys.**24**, 79(1952).https://doi.org/10.1103/RevModPhys.24.79

[22] W. H. Miller, M. Diaz de Leon, Utilization of phoswich detectors for simultaneous, multiple radiation detection.J. Radioanal. Nucl. Chem.**264**, 163-167(2005).https://doi.org/10.1007/s10967-005-0689-6

[23] Leo W R, *Techniques for nuclear and particle physics experiments: a how-to approach*.(Springer Science & Business Media, 1994), pp.189-190

[24] M. Yoneyama, J. Kataoka, M. Arimoto, *et al.*, Evaluation of GAGG:Ce scintillators for future space applications.J. Instrum.**13**, (2018).10.1088/1748-0221/13/02/P02023

[25] H.Y. Wu, Z.H. Li, H. Tan, *et al.*, A general-purpose digital data acquisition system (GDDAQ) at Peking University.Nucl.Instrum. Methods Phys.Res.A.**975**, 164200(2020). https://doi.org/10.1016/j.nima.2020.164200

[26] H.Y. Wu, Z.H. Li, H. Tan, *et al.*, A general-purpose data acquisition system and a pulse analysis algorithm based on digitization (in Chinese).Chin.Sci.Bull.**66**, 3553-3560(2021).10.1360/TB-2021-0552

[27] Di-Wen Luo, Hong-Yi Wu, Zhi-Huan Li, *et al.*, Performance of digital data acquisition system in gamma-ray spectroscopy.Nucl. Sci. Tech.**32**, 79(2021). 10.1007/s41365-021-00917-8

[28] A. Al-Adili, F.-J. Hambsch, S. Oberstedt, *et al.*, Comparison of digital and analogue data acquisition systems for nuclear spectroscopy.Nucl.Instrum. Methods Phys.Res.A.**624**, 684-690(2010).https://doi.org/10.1016/j.nima.2010.09.126

[29] Hao Cheng, Bao-Hua Sun, Li-Hua Zhu, *et al.*, Intrinsic background radiation of $LaBr_3$(Ce) detector via coincidence measurements and simulations.Nucl. Sci. Tech.**31**, 99-

(2020).https://doi.org/10.1007/s41365-020-00812-8

[30] B.D. Milbrath, R.C. Runkle, T.W. Hossbach, *et al.*, Characterization of alpha contamination in lanthanum trichloride scintillators using coincidence measurements.Nucl.Instrum. Methods Phys.Res.A.**547**, 504-510(2005). https://doi.org/10.1016/j.nima.2004.11.054

[31] Y. -Y. Ji, H. -Y. Choi, Wanno Lee, *et al.*, Application of a LaBr3(Ce) Scintillation Detector to an Environmental Radiation Monitor.IEEE Trans. Nucl. Sci. **65**, 2021-2028(2018).10.1109/TNS.2018.2823322

[32] Allison, J, Amako, K, J. Apostolakis, *et al.*, Recent developments in Geant4. Nucl.Instrum. Methods Phys.Res.A. **835**, 186-225(2016). https://doi.org/10.1016/j.nima.2016.06.125

[33] Allison J, Amako K, Apostolakis J E A, *et al.*, Geant4 developments and applications. IEEE Trans. Nucl. Sci. **53**, 270-278(2006). 10.1109/TNS.2006.869826

[34] Qiao C K, Wei J W, Chen L, An overview of the compton scattering calculation. Cryst. **11**, 525(2021). https://doi.org/10.3390/cryst11050525

[35] Prashant Shukla and Sundaresh Sankrith, Energy and angular distributions of atmospheric muons at the Earth.Int. J. Mod. Phys. A.**33**, 1850175(2018). https://doi.org/10.1142/S0217751X18501750

[36] Bryan Olmos Yáñez and Alexis A. Aguilar-Arevalo, A method to measure the integral vertical intensity and angular distribution of atmospheric muons with a stationary plastic scintillator bar detector. Nucl. Instrum. Methods Phys. Res. A. **987**, 164870(2021).https://doi.org/10.1016/j.nima.2020.164870

[37] Xia Haihong, Zhu Lihua, Huang Zheng-de, *et al.*, Study of Giant Dipole Resonance in Hot Rotating Nuclei.Nucl.Phys.Rev.**15**, 266-273(1998).DOI: 10.11804/NuclPhysRev.15.04.266

[38] Bai J H, Niu Z M, Sun B Y, *et al.*, The description of giant dipole resonance key parameters with multitask neural networks. Phys. Lett. B. **815**, 136147(2021).https://doi.org/10.1016/j.physletb.2021.136147